

Investigation of Polyacrylonitrile-Derived Multiple Carbon Shell Composites for Silicon-Based Anodes in Lithium-Ion Batteries

Lukas Alexander Dold,^{*,[a]} Chinmay Rajeev Bapat,^[a] Harald Gentischer,^[a] Niklas Ortlieb,^[b] Anna Fischer,^{*,[b, c]} Kai Peter Birke,^[d] and Daniel Biro^[a, c]

The aim of manufacturing silicon-carbon (Si/C) composites for lithium-ion batteries is to embed silicon particles into a carbon matrix or shell, which results in improved electrical conductivities and cycling stability by avoiding the direct solid electrolyte interphase (SEI) formation on the silicon surfaces. In this study, we explore the production of Si/C composites containing one (single) and two (multiple) carbon shells, achieved through the carbonization of polyacrylonitrile. We thoroughly analyze the carbonization process of polyacrylonitrile and investigate the structural, physical, and electrochemical properties of the resulting Si/C composites. Our findings indicate that the

increase of the carbon fraction and the second thermal treatment during the manufacturing of multiple carbon shells (MCS) have a significant impact on the conductivity of the powders, increasing it by one order of magnitude. We also discover that the MCS cover the silicon surface more effectively, as revealed through etching in a NaOH solution and subsequent elemental analysis. The MCS composite, containing 30 wt.% silicon, exhibits the best cycling performance in half-cells at 0.5 C, with an initial capacity of 776 mAhg⁻¹ and a capacity retention of 83.0% after 100 cycles.

Introduction

Silicon-based anodes have been attracting growing attention to be the most promising candidate for the next-generation anode material of high energy density lithium-ion batteries.^[1–4] Silicon is abundantly available, possesses a theoretical specific capacity of 3578 mAhg⁻¹ (Li₁₅Si₄) nearly ten times higher than that of graphite (372 mAhg⁻¹) and has a low working potential of 0.2–0.4 V vs. Li/Li⁺.^[5] However, during (de-)lithiation silicon

particles experience a huge volume change of 280% which causes particle pulverization through electrochemical milling and continuous disruption and reformation of the solid electrolyte interphase (SEI) on the surface of the newly exposed areas.^[2] This results in irreversible consumption of lithium-ions and electrolyte constituents and the rise in cell polarization due to the insulating effect of a thick SEI layer, all leading to a fast capacity decay.^[6–8]

To overcome these challenges several approaches have been developed including nanosized or nanostructured active materials,^[9] modified binders,^[10,11] pre-lithiation,^[12] electrolyte additives^[13] and carbon surface coatings.^[8] Carbon coatings can be achieved by dispersing silicon particles in organic carbon sources such as pitch, mono- and polysaccharides or polymers followed by a subsequent thermal treatment to carbonize and graphitize these substances.^[8,14]

Studies using electrically conductive polymers such as polyacrylonitrile (PAN) or polyaniline (PANI) as the carbon source in such silicon-containing composites have shown improved capacity retentions.^[15–20] Polyacrylonitrile is used as a carbon source for the manufacturing of silicon-carbon composites due to its high carbon content, excellent electronic conductivity of carbonized PAN, absence of oxygen in the carbon source, and wide availability due to the broad industrial application for the manufacturing of high-tensile carbon.^[21,22] Upon thermal treatment between 180 °C and 425 °C the acrylonitrile units of PAN undergo exothermic cyclization and conjugation reactions forming connected ring compounds.^[23] For PAN homopolymers this reaction follows the free radical mechanism described by Kim et al.^[24] Successive heating (425 °C–600 °C) leads to dehydrogenation and crosslinking in the lateral direction. At temperatures beyond 600 °C carbon-

[a] L. A. Dold, C. R. Bapat, H. Gentischer, Dr.-Ing. D. Biro
Department of Electrical Energy Storage
Fraunhofer Institute for Solar Energy Systems ISE
Heidenhofstraße 2, 79110 Freiburg (Germany)
E-mail: lukas.alexander.dold@ise.fraunhofer.de

[b] N. Ortlieb, Prof. Dr. A. Fischer
Institute for Inorganic and Analytical Chemistry (IAAC)
University of Freiburg
Albertstraße 21, 79104 Freiburg (Germany)
E-mail: anna.fischer@ac.uni-freiburg.de

[c] Prof. Dr. A. Fischer, Dr.-Ing. D. Biro
Freiburger Materialforschungszentrum (FMF)
University of Freiburg
Stefan-Meier-Straße 21, 79104 Freiburg (Germany)

[d] Prof. Dr.-Ing. K. P. Birke
Chair for Electrical Energy Storage Systems
Institute for Photovoltaics (ipv)
University of Stuttgart
Pfaffenwaldring 47, 70569 Stuttgart (Germany)

Supporting information for this article is available on the WWW under <https://doi.org/10.1002/batt.202400012>

© 2024 The Authors. Batteries & Supercaps published by Wiley-VCH GmbH. This is an open access article under the terms of the Creative Commons Attribution License, which permits use, distribution and reproduction in any medium, provided the original work is properly cited.

ization takes place through the elimination of nitrogen as several volatile compounds.^[23,25,26]

This makes PAN a promising candidate to be used in silicon carbon composites (Si/C) that are either processed at moderate temperatures to achieve an intrinsic conductive polymer matrix with conjugated double bonds or being carbonized at temperatures $> 600\text{ }^{\circ}\text{C}$. Piper et al.^[27] dispersed silicon nanoparticles in a PAN solution using a ratio of 7:3 (Si: PAN) and cast the as achieved slurry on a copper current collector. Subsequently the electrodes were thermally treated at $300\text{ }^{\circ}\text{C}$ – $500\text{ }^{\circ}\text{C}$ to cyclize the PAN while avoiding carbonization reactions. Initially high specific capacities of 2585 mAh g^{-1} and a capacity retention of 58% after 150 cycles at 0.1 C were related to the intrinsic electrical conductivity of the delocalized $sp^2\ \pi$ bonds formed during cyclization and the remaining polymeric properties of PAN due to limited pyrolysis. Datta and Kumta^[19] synthesized silicon-graphite-polyacrylonitrile composites containing 17.5 wt.% silicon at $800\text{ }^{\circ}\text{C}$ in argon atmosphere for four hours, exhibiting a reversible capacity of $\sim 660\text{ mAh g}^{-1}$ cycled at a rate of $\sim 0.25\text{ C}$.

Despite covering the silicon nanoparticle surfaces using a carbon source such as polyacrylonitrile or others, many Si/C composites suffer from a fast capacity fade during the initial cycles before achieving stable specific capacities.^[8] This leads to the hypothesis that a simple single carbon coating on the surface of the silicon particles does not overcome the challenges comprising of internal fracturing and SEI thickening, to achieve a sufficient capacity retention. Liu et al.^[28] showed an improved cycling performance of their double carbon coated multi-core yolk-shell mesoporous composite structure achieved through a sol-gel process, compared to their single carbon coated composite. This was attributed to improved conductivity. Vrankovic et al.^[29] embedded mesoporous crystalline silicon either into a fructose-derived carbon shell or a polymer-derived SiOC ceramic. Both composites resulted in high initial capacities but only a matrix including both the fructose-derived carbon and SiOC, resulted in a stable cycling behavior over 50 cycles (capacity retention 91% compared to 49% for the silicon stabilized solely in the SiOC matrix). The superior performance was related to a better protection of the silicon surface from the electrolyte and an improved electrode integrity.

Herein, we present our most recent findings on the impact of multiple carbon shells in silicon-based composites for anodes in lithium-ion batteries. To be able to relate the electrochemical performance directly to the effects of a single or two step

carbon coating process we use polyacrylonitrile as the only carbon source in both steps to avoid impacts caused by different carbon precursors. In our study we manufactured Si/C composites containing either single or multiple carbon shells and evaluated their structural and electrochemical properties. Thermogravimetric Analysis (TGA) and Differential Scanning Calorimetry (DSC) were used to evaluate the thermal decomposition of polyacrylonitrile. The chemical structure of the composites was analyzed using Fourier-transform infrared spectroscopy (FTIR), Raman spectroscopy, X-ray diffraction (XRD) and elemental analysis. Additionally, the composites were characterized regarding their specific surface area and pore volume distribution using nitrogen physisorption measurement and the particle morphology was investigated using scanning electron microscopy (SEM) and scanning electron microscopy in transmission mode (SEM-TE). To complete the physicochemical characterization of the composites the electric conductivity was measured. The electrochemical performance as anode active material for lithium-ion batteries was investigated in half-cells using a lithium counter electrode. While the usage of higher carbon contents for single carbon coated composites did not lead to an improved capacity retention (69.0% for a 23.9 wt.% carbon fraction and 66.7% for a 43.5 wt.% carbon fraction after 100 cycles respectively), two step carbon coated composites showed a reduced capacity fade especially for increased carbon content in the second coating step (capacity retention of 83.0% after 100 cycles). In addition to an improved capacity retention, the multiple carbon shell composites were found to have higher electric conductivities (powder samples) and reduced impedances during cycling in cells. We were able to relate these effects to a better carbon coverage of the silicon particle surface, revealed by etching experiments in combination with elemental analysis.

Results and Discussion

Structural Properties of Single and Multiple Carbon Shell Composites

Figure 1 presents the synthesis scheme and a schematization of the morphology of the composite materials evaluated within this work.

Si/C composites consisting of a single carbon shell (Si@SCS) or multiple carbon shells (Si@MCS) were prepared. For single

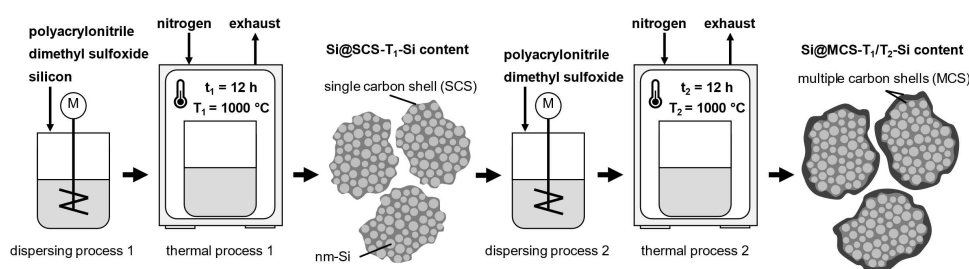


Figure 1. Schematic overview of the synthesis process of Si@SCS and Si@MCS composites.

composite	Si: PAN ratio 1st thermal process	Duration and temperature 1st thermal process	Si: PAN ratio 2nd thermal process	Duration and temperature 2nd thermal process
Si@SCS-1000-70	1:1	12 h @ 1000 °C	–	–
Si@SCS-1000-50	1:2	12 h @ 1000 °C	–	–
Si@MCS-1000/1000-50	1:1	12 h @ 1000 °C	1:1	12 h @ 1000 °C
Si@MCS-1000/1000-30	1:1	12 h @ 1000 °C	1:5	12 h @ 1000 °C

carbon shell (SCS) composites polyacrylonitrile was dissolved in dimethyl sulfoxide and mixed with silicon nanoparticles, followed by a thermal process to pyrolyze the carbon source. Multiple carbon shell composites were prepared by dispersing the Si@SCS-1000-70 ("SCS" for single carbon shell, "1000" for 1000 °C in the thermal process step and "70" for 70 wt.% silicon in the final composite) composite in a second polyacrylonitrile solution, followed by a second thermal treatment at the same temperature. The used mass ratios for the composite synthesis were selected according to Table 1.

The thermal conversion processes of pristine polyacrylonitrile, a silicon nanoparticle polyacrylonitrile dispersion (corresponding to the thermal process to achieve SCS composites) and a Si@SCS-1000-70 polyacrylonitrile dispersion (corresponding to the thermal process to achieve MCS composites) were analyzed using simultaneous TGA and DSC measurements under nitrogen flow (Figure 2a) + b)) between room temperature and 1000 °C. The dispersed samples were achieved by dispersing the powders in DMSO and subsequently drying them at 80 °C under vacuum. For the pristine PAN sample, the cyclization reaction can be observed at the initiation of the

mass reduction (TGA) and the exothermic peak in the DSC measurement at 256.1 °C, which is in line with the literature values for cyclization between 180 °C and 425 °C.^[23,26] The samples containing silicon and the Si@SCS-1000-70 composite show a similar behavior with slightly shifted reaction peaks (cyclization peak at 264 °C and 269 °C respectively). The TGA curves for these samples reveal a mass loss starting at 120 °C possibly due to the evaporation of solvent residues and catalytic effects of the silicon nanoparticles having a specific surface area of 32 m²g⁻¹. The broad decomposition region between 500 °C and 1000 °C resembles the reactions taking place due to successive heating, such as dehydrogenation (425–600 °C for PAN), lateral crosslinking of the polymer structures through nitrogen elimination (> 600 °C for PAN) as volatile compounds.^[23,25,26] While the dehydrogenation and nitrogen elimination can be differentiated by two broad peaks for the pristine PAN sample these reactions seem to overlap for the samples containing silicon. Since there is still a detectable heat flow at 1000 °C for all three samples it is evident that to complete the carbonization higher temperatures would be needed. This is in good accordance with literature using

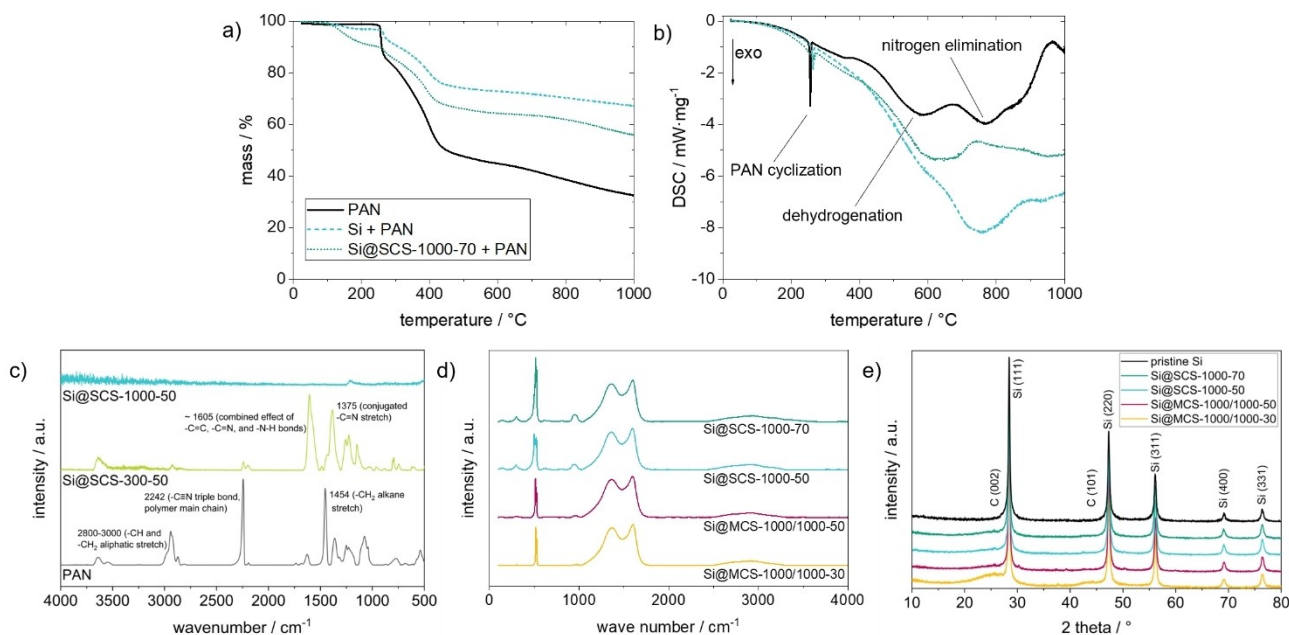


Figure 2. a) TGA and b) DSC curves recorded for PAN, Si + PAN and Si@SCS-1000-70 + PAN between room temperature and 1000 °C under nitrogen flow at a heating rate of 1 K min⁻¹, c) FTIR spectra recorded for pristine PAN, Si@SCS-300-50 and Si@SCS-1000-50, d) Raman spectra normalized by the peak of the G-band and e) XRD patterns of the Si/C composites.

thermal processes at $> 1000\text{ }^{\circ}\text{C}$ for carbon nanofiber production derived from polyacrylonitrile.^[25,26,30]

To characterize the morphological and chemical properties of the Si/C composites, FTIR spectroscopy, Raman spectroscopy, X-ray diffraction (XRD), elemental analysis (EA), N_2 -adsorption and conductivity measurements were conducted. Figure 2 c) shows the FTIR spectra measured for pristine PAN, a silicon PAN (1:1 by weight) mixture treated at $300\text{ }^{\circ}\text{C}$ for 12 hours (Si@SCS-300) and the Si@SCS-1000-50 composite. The pristine PAN shows characteristic adsorption bands at $2800\text{--}3000\text{ cm}^{-1}$, 2240 cm^{-1} , 1454 cm^{-1} due to CH and CH_2 aliphatic stretches, carbon nitrogen triple bond and CH_2 alkane stretch respectively. For the Si@SCS-300 sample the carbon nitrogen triple bond absorption band at 2242 cm^{-1} is reduced compared to the pristine PAN, while absorption bands at 1605 cm^{-1} and 1375 cm^{-1} corresponding to carbon-carbon and carbon-nitrogen double bonds are visible, corroborating with the literature findings of the cyclization having taken place during the thermal process.^[24] No absorption band of relevant intensity is visible for the Si@SCS-1000-50 sample indicating the carbonization of the composite.

Raman spectroscopy (Figure 2 d)) was therefore conducted to analyze the carbon structure of the manufactured SCS and MCS composites. The sharp band at $\sim 500\text{ cm}^{-1}$ and the band at $\sim 950\text{ cm}^{-1}$ are visible for all four samples and correspond to the silicon in the composites. The D_1 -band at $\sim 1345\text{ cm}^{-1}$ and the G-band at $\sim 1590\text{ cm}^{-1}$ correspond to defect-rich graphene sheets (D_1) and the in-plane vibrations of carbon atoms in the graphene network (G). The obtained spectra were fitted using a mixed Gaussian-Lorentzian approach (Figure S1, Supporting Information). The three other bands correspond to single graphene layers or top layers of graphite stacks (D_2 , $\sim 1670\text{ cm}^{-1}$), amorphous carbon structures (D_3 , $\sim 1540\text{ cm}^{-1}$) and sp^2 -carbon bound to sp^3 -carbon (D_4 , $\sim 1190\text{ cm}^{-1}$).^[31] A degree of graphitization of 9.3% to 14.3% was calculated for the four composites by dividing the area of the G-band by the total area of all bands (Table S1, Supporting Information). The overtones of the D and G bands are visible at wave numbers

$> 2500\text{ cm}^{-1}$. The slightly higher degrees of graphitization of the two SCS composites are attributed to the catalytic effect of silicon nanoparticles on graphitization. The catalytic effect of silicon-based nanoparticles has been observed in previous publications.^[32,33] The reduced degrees of graphitization in MCS composites are explained by the fact that the carbon in the second carbon shell has a smaller contact area with the silicon nanoparticles than the first carbon shell. For polyacrylonitrile carbonized without silicon (PAN-1000), a degree of carbonization of 8.4% was calculated (Table S1, Supporting Information). Comparing this value with the degrees of carbonization of the SCS composites (14.3% for the Si@SCS-1000-70 and 14.2% for the Si@SCS-1000-50) confirms the catalytic effect of silicon nanoparticles on the graphitization of polyacrylonitrile.

Additionally, X-ray diffraction (XRD) measurements of the Si/C composites and the pristine silicon were performed. The X-ray patterns of all four composites in Figure 2e) indicate that the embedding into the carbon matrix and the subsequent thermal treatment did not result in the formation of electrochemically inactive silicon carbide. Especially for the Si@MCS-1000/1000-30 composite the C (002) and C (101) reflections of the carbon shells are visible.

Scanning electron microscope images provide an insight into the particle morphology. The bulk overview images in Figure 3 reveal that for all four composites micrometer sized particles are obtained (an image of the pristine silicon nanoparticles is shown in Figure S2, Supporting Information). While the particles of all composites have an angular shape, caused by the fractured edges in the ball milling process, the surface roughness differs depending upon the carbon fraction of the composites. The spherical silicon nanoparticles can be observed in all four composites but are visible best in the Si@SCS-1000-70 composite due to the lowest carbon fraction leading to a rough particle surface. With an increasing carbon fraction, the carbon seems to dominate the particle surface, covering the single silicon particles and reducing the particle surface roughness.

SEM-TE was conducted to reveal the core shell structure of the composites (Figure 4). A Si@MCS-1000/1000-30 sub- μm

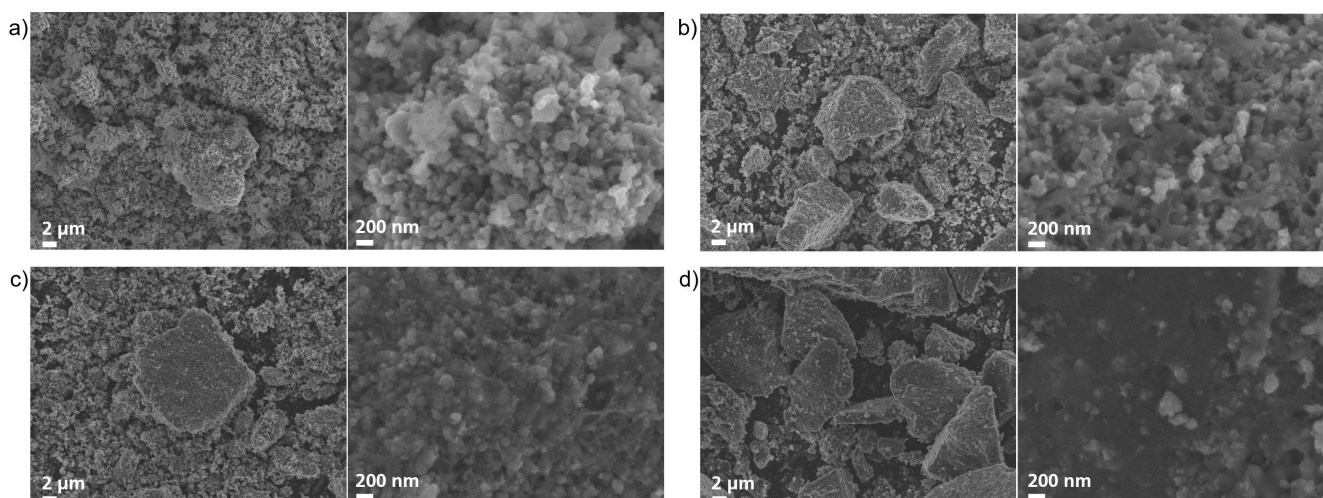


Figure 3. Scanning electron microscopy micrographs of a) Si@SCS-1000-70 b) Si@SCS-1000-50 c) Si@MCS-1000/1000-50 and d) Si@MCS-1000/1000-30.

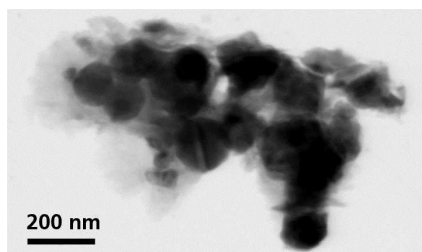


Figure 4. SEM-TE micrograph of a sub- μm Si@MCS-1000/1000-30 particle.

particle was selected for the measurement revealing the presence of spherical silicon nanoparticles covered by a carbon shell.

While the SEM and SEM-TE images reveal the presence of carbon on the silicon particle surface for the analyzed particles, it cannot be determined whether all silicon particles are fully covered by a carbon shell. In addition to that, a full coverage of the silicon particles might not be sufficient if the carbon shell consists of a highly porous structure. Therefore, a parameter to estimate the amount of silicon still accessible for the electrolyte is of high interest.

To estimate this parameter, we conducted etching experiments in aqueous NaOH solutions followed by elemental analysis. Si/C composites (500 mg) were stirred in a 0.25 M NaOH solution (8 ml) for 48 h. The samples were subsequently filtered, washed with deionized water three times and dried at 40 °C. To determine the carbon content (before and after etching) as well as remaining hydrogen and nitrogen fractions of all composite samples and pristine polyacrylonitrile, elemental analysis (C, H, N and S) was conducted.

In good accordance with the Si: PAN ratios used during the composite synthesis process; different carbon fractions were measured (Table 2). Nitrogen fractions of 2.8–4.0 wt.% indicate that the elimination of nitrogen as volatile compounds during

the carbonization process is not completed and would need higher temperatures or longer processing times. This was already presumed based on the heat flow shown in the DSC curves (Figure 2 b)). For reference, the Elemental Analysis of pristine polyacrylonitrile and carbonized polyacrylonitrile (PAN-1000, thermal process according to SCS composites without adding silicon to the dispersion) are listed in Table 2 as well. The pristine polyacrylonitrile shows a residual fraction of 0.9 wt.% which we attribute to impurities such as catalysts and byproducts from the polymerization. Some of these impurities seem to not decompose or volatilize during the thermal process resulting in the residual fraction of the carbonized polyacrylonitrile.

Assuming the residue of the Elemental Analysis of the composites attributes fully to the silicon particles and their oxide layers, whose masses stay unaffected during thermal treatment, a mass loss of ~ 61.5 wt.% (average value calculated for all four composites) can be calculated for polyacrylonitrile during the carbonization in the thermal processes at 1000 °C for 12 hours. Based on the residual fractions before ($w_{\text{residual,be}}$) and after etching ($w_{\text{residual,ae}}$) the fraction of silicon not fully covered ($w_{\text{Si,etched}}$) by the carbon matrix can be calculated using equation 1 (Table 3). To eliminate potentially evolved oxygenic functionalization of the carbon structure during the dispersing and etching experiment, the dried samples were also heated to 1000 °C and held for 12 h. By comparing the elemental composition before and after this additional temperature treatment it was found that oxygenic functionalization did not occur during the etching (Table S2, Supporting Information). It was found that the single carbon shell composites did not lead to an adequate coverage of the silicon surface since 37.1 wt.% and 44.3 wt.% of the silicon were etched in the NaOH solution for the Si@SCS-1000-70 and Si@SCS-1000-50 samples respectively. The higher carbon fraction in the Si@SCS-1000-50 composite did not improve the silicon coverage. However, the two multiple carbon shell composites show remarkably lower values

Table 2. Elemental Analysis of pristine polyacrylonitrile and the composites.

composite	C/wt.%	H/wt.%	N/wt.%	S/wt.%	residual/wt.%
polyacrylonitrile	68.8	4.8	24.8	0.3	1.3
PAN-1000	92.8	0.0	4.5	0.3	2.4
Si@SCS-1000-70	23.9	0.3	2.8	0.3	72.7
Si@SCS-1000-50	43.5	0.9	3.5	0.3	51.8
Si@MCS-1000/1000-50	39.2	1.2	3.6	0.5	56.0
Si@MCS-1000/1000-30	66.1	0.0	4.0	0.2	29.7

Table 3. Residual fraction of Si/C composites before and after NaOH etching calculated from Elemental Analysis.

etched composite	$w_{\text{residual,be}}$ /wt.%	$w_{\text{residual,ae}}$ /wt.%	$w_{\text{Si,etched}}$ /wt.%
Si@SCS-1000-70	72.7	45.7	37.1
Si@SCS-1000-50	51.8	28.8	44.3
Si@MCS-1000/1000-50	56.0	47.4	15.2
Si@MCS-1000/1000-30	29.7	30.1	-1.4

of 15.2 wt.% for the Si@MCS-1000/1000-50 and -1.4 wt.% for the Si@MCS-1000/1000-30 composite. The negative value for the Si@MCS-1000/1000-30 composite is attributed to slight inhomogeneities of the active material and potential measurement errors and can be interpreted as a carbon coverage that prevents the silicon particles from contact with the NaOH and hence with the electrolyte.

$$W_{Si,etched} = 1 - \frac{W_{residual,ae}}{W_{residual,be}} \cdot 100 \% \quad (1)$$

To investigate the specific surface area, pore volume and pore size distribution of the pristine and etched composites, N_2 -adsorptions measurements were conducted. Brunauer-Emmett-Teller (BET) and the quenched solid density functional theory were applied. The four pristine composites reveal low specific surface areas, ranging from approximately $6 \text{ m}^2 \text{ g}^{-1}$ to $48 \text{ m}^2 \text{ g}^{-1}$ and low pore volumes, ranging from approximately $0.009 - 0.0650 \text{ cm}^3 \text{ g}^{-1}$ (Table 4). Increased specific surface areas and pore volumes are observed for the two NaOH treated single carbon shell composites due to a decent amount of silicon being etched during that process. The adsorption isotherms (Figure S3, Supporting Information) follow type IV, indicating

the presence of meso- and micropores, that is typically observed in materials having slit-shaped or cylindrical pores. The hysteresis of the type IV isotherm is attributed to capillary condensation during the measurement.^[34] While the presence of these pores can lead to improved electrolyte penetration and faster reaction kinetics, enhanced surface area leads to an increase in SEI formation and irreversible lithium losses. The separation into fractions of micro- and mesopores is shown in Table 4.

To visualize the effects of the NaOH etching experiments on the composites, scanning electron microscope images were taken. All composites in Figure 7 reveal a changed structure compared to the pristine materials in Figure 5. Spherical holes evolve on the composite surface at places where the spherical silicon nanoparticles, that were not fully covered by the carbon shell, were etched away from the particle. As expected, based on the residual fractions calculated from Elemental Analysis in Table 3 these holes are visible in larger numbers for the single carbon shell composites. It needs to be mentioned that the NaOH etching is not capable of determining precise values for the percentage share of silicon surface not covered by the carbon shell, since partly covered particles are still fully etched by this treatment. However, this simple method is still capable

Table 4. Specific surface area (BET) and QSDFT calculated pore volume of the pristine and etched Si/C composites.

composite	specific surface area/ $\text{m}^2 \text{ g}^{-1}$	micropore surface area (pore size < 2 nm)/%	pore volume/ $\text{cm}^3 \text{ g}^{-1}$	micropore volume (pore size < 2 nm)/%
Si@SCS-1000-70	40.41	15.29	0.0648	5.85
Si@SCS-1000-50	41.29	3.77	0.0629	1.29
Si@MCS-1000/1000-50	48.43	34.57	0.0623	13.13
Si@MCS-1000/1000-30	6.51	5.76	0.0087	3.59
Si@SCS-1000-70_etched	67.10	41.99	0.1077	11.76
Si@SCS-1000-50_etched	93.00	50.20	0.1211	18.28
Si@MCS-1000/1000-50_etched	46.72	43.49	0.0543	17.93
Si@MCS-1000/1000-30_etched	2.68	37.76	0.0050	9.43

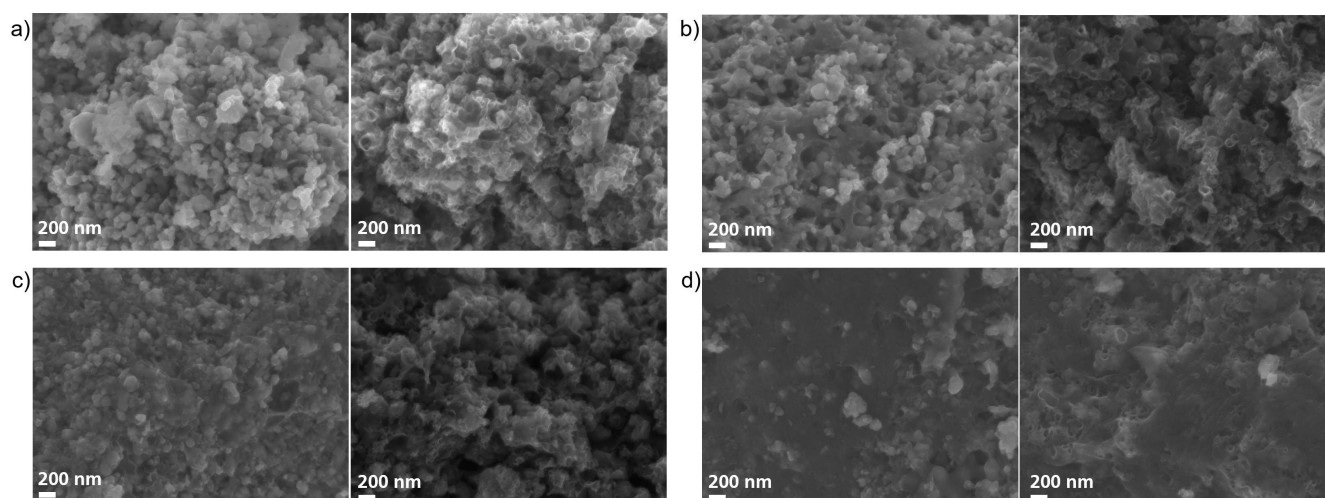


Figure 5. Scanning electron microscopy micrographs of pristine (left) and etched (right) composites a) Si@SCS-1000-70 b) Si@SCS-1000-50 c) Si@MCS-1000/1000-50 and d) Si@MCS-1000/1000-30.

of indicating the quality of the silicon embedment, especially since composite manufacturing processes should aim for a full coverage of the silicon surface area.

To finalize the characterization of the structural properties, the electrical conductivity of the composite powders was determined via electrochemical impedance spectroscopy (EIS). Figure 6 reveals that with increasing pressure all four composites show a linear increase in the electrical conductivity due to particle compression. When comparing the two SCS composites (Si@SCS-1000-50 and Si@SCS-1000-70) or the two MCS composites (Si@MCS-1000/1000-50 and Si@MCS-1000/1000-30), an increased electronic conductivity can be observed for the composites with the higher carbon content, which confirms the influence of the carbon content on the electronic conductivity. The lowest specific electronic conductivity was achieved for the composite with the lowest carbon fraction with one thermal treatment step (Si@SCS-1000-70). Comparing Si@SCS-1000-50 and Si@MCS-1000/1000-50 it was found that the MCS composite has an increased specific conductivity. In Figure S4

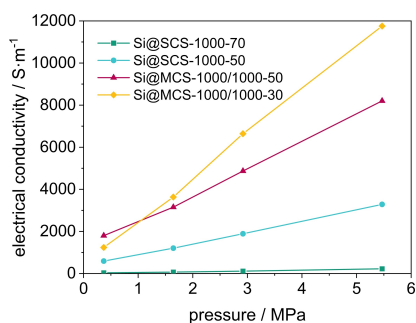


Figure 6. Specific conductivity depending on the applied pressure for the Si/C composites.

(Supporting Information) it is revealed that a second thermal treatment (further carbonization of the composite) of the Si@SCS-1000-50 composite without the addition of more PAN increases the specific conductivity towards the values of the Si@MCS-1000/1000-50 composite. This is in good accordance with literature showing an increase in electric conductivity for polyacrylonitrile with successive carbonization.^[26] Despite an increase in electronic conductivity, no improved electrochemical performance could be achieved for the Si@SCS-1000/1000-50 composite compared to the Si@SCS-1000-50 composite (Figure S5, Supporting Information).

To conclude, the data shows that the specific electronic conductivity of the active materials can be increased by both an increased carbon content and a second thermal process step.

Electrochemical Properties of Si@SCS and Si@MCS Composites

To investigate the electrochemical performance of the Si/C composites constant current constant voltage cycling (CCCV) and electrochemical impedance spectroscopy were conducted. In accordance with the carbon content in the composites, different initial capacities were achieved for the four materials (Figure 7). The Si@SCS-1000-70 shows the highest initial delithiation capacity of 1905 mAh g^{-1} . Decreasing the silicon content to $\sim 50 \text{ wt.}\%$ for the Si@SCS-1000-50 and Si@MCS-1000/1000-50 leads to initial delithiation capacities of 1454 mAh g^{-1} and 1516 mAh g^{-1} respectively. The Si@MCS-1000/1000-30 contains the highest carbon fraction and therefore results in the lowest initial capacity of 776 mAh g^{-1} . Interestingly, the first cycle efficiency is higher for the SCS composites and decreases with increasing carbon content resulting in a lithiation

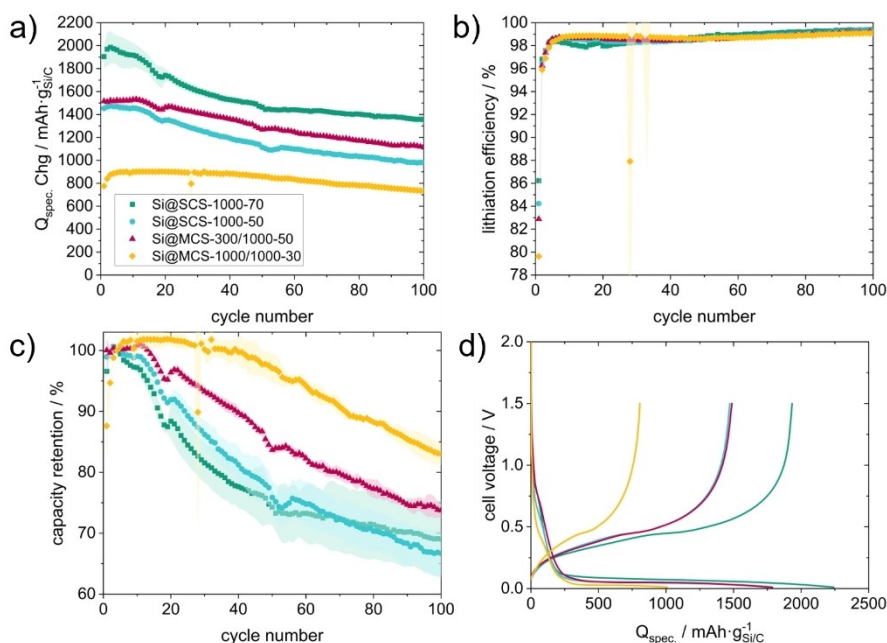


Figure 7. Constant current constant voltage cycling measurement of Si@SCS and Si@MCS composites vs. Li/Li^+ at a rate of 0.5 C between 0.01 V and 1.5 V. a) specific charge capacity, b) lithiation efficiency, c) capacity retention and d) voltage curve of the first formation cycle.

efficiency of 86.2% for Si@SCS-1000-70, 84.2% for Si@SCS-1000-70, 82.9% for Si@MCS-1000/1000-50 and 79.6% for Si@MCS-1000/1000-30 (Figure 7 b)). SEI formation attributes to these losses for all four composites but seems to be only one of the factors since the Si@MCS-1000/1000-30 with the lowest specific surface area shows the lowest initial lithiation efficiency. However, the initial lithiation efficiencies correlate with the degree of graphitization of the carbon content of the composites, which was calculated from the Raman spectra (Table S1, Supporting Information). A lower degree of graphitization results in higher initial losses due to lithium trapping in the amorphous carbon structures. Previous studies have shown correlations between the electrolyte-accessible surface area, quantified by the specific surface area of the active material, and the initial lithiation losses, as well as between the degree of graphitization and the specific capacity and reversibility of the initial lithiation.^[36–38] Furthermore, there are also publications on methods to counteract these initial losses by increasing the degree of graphitization through the use of catalysts or compensating for lithium loss through pre-lithiation.^[35,38,39]

The 1st cycle voltage vs. capacity curves of the formation cycle of the four composites reveals a slight plateau at ~0.75 V corresponding to the SEI formation of the first cycle. The decomposition voltages of the electrolyte components are within the potential window between 0.5 V and 2.25 V vs. Li/Li⁺.^[40] Figure 7 d) indicates reduced reactions and therefore reduced SEI formation of the Si@MCS-1000/1000-30 within this potential window. To provide a clearer illustration, differential capacity analysis was applied to the measurement data within this potential window, as shown in Figure S6 (Supporting Information). A smaller peak area of the Si@MCS-1000/1000-30 can be associated with less charge consumed by SEI formation and is in good accordance with the lower specific surface area compared to the other active materials (Table 4).

To compare the degradation properties of the composites with different initial specific capacities the capacity retention shown in Figure 7 c) is considered. The data graphs showing the specific capacity and the capacity retention of the four composites can be divided into two regions. Initially, there is a phase of stable specific capacity (capacity retention > 98%), which is maintained for different numbers of cycles for each composite. For Si@MCS-1000/1000-30, this phase is most pronounced and extends over the first 46 cycles, while stable capacity retention for Si@SCS-1000-70 only extends over seven cycles. In the subsequent second region, a significant decline in capacity is observed. In terms of lithiation efficiency (Figure 7 b)), the region of high cycle stability is characterized by an increasing or high lithiation efficiency over the cycles, while it is reduced in the region of capacity loss. This is particularly evident in the behavior of Si@MCS-1000/1000-30. The degradation behavior in the second region is attributed to pulverization of the composite material due to the breaking of the carbon shell caused by mechanical stresses from the volume expansion of silicon during lithiation. The electronic isolation of individual particle fragments as well as the reformation of the SEI on the exposed composite surfaces result in the reduced lithiation efficiency of the active materials.

The data of the two single carbon shell composites look similar indicating the same degradation mechanisms. This leads to the result that an increase of the carbon fraction within the evaluated range does not improve the cycling stability of the SCS composites (capacity retentions of 69.0% for the Si@SCS-1000-70 and 66.7% for the Si@SCS-1000-50 composite after 100 cycles). Looking at the SCS and MCS composites with a 50 wt.% silicon fraction it can be stated that the Si@MCS-1000/1000-50 composite shows slightly improved cycling performance over the first 80 cycles. The Si@MCS-1000/1000-30 composite does show the best performance having a capacity retention of 83.0% after 100 cycles. When comparing the capacity retention of the two MCS composites, the influence of the carbon content on the electrochemical performance of the active material becomes apparent. The better embedding of silicon particles in Si@MCS-1000/1000-30 appears to enhance the mechanical stability of the composite. In Figure S5 (Supporting Information), the electrochemical performance of a Si@SCS-1000-30 composite is shown to demonstrate that the improved cycling stability is attributed to the second carbon shell and not just the increased carbon content. However, it is also evident that the carbon structure is not able to fully counteract the degradation mechanisms, although a significant improvement in cycle stability can be achieved. This provides a starting point for further development of the composite material. The literature shows that the mechanical stresses on the composite can be reduced, for example, by introducing void structures, which can further enhance cycle stability.^[41–43]

The described degradation effects of SEI growth and composite particle fracturing lead to an increase in cell impedance, which was investigated using electrochemical impedance spectroscopy. Figure 8 shows the Nyquist-Plots of the electrochemical impedance spectroscopies performed after formation and cycling. A decrease in cell impedance over the first ten cycles can be observed for the Si@SCS-1000-50 and both MCS composites. This is in good accordance with the cycling stability of these active materials in these cycles. Although the Si@SCS-1000-70 composite has the lowest impedance after the formation cycle, a tremendous increase can be observed over the first ten cycles proving the assumed degradation mechanisms such as composite particle break-up and SEI growth. In contrast, the Si@MCS-1000/1000-30 composite shows a higher impedance after formation possibly due to the higher amorphous carbon content referred to previously. However, this impedance reduces significantly during the subsequent ten cycles and proves to be the lowest amongst the four materials after 30 cycles. Therefore, it could be stated that the presence of the multiple carbon shells with a higher carbon content helped embedding the silicon particles better to allow a more stable SEI layer formation and mitigate lithium losses from various degradation mechanisms noted previously. The impedances of the other two evaluated materials, lie in between the values of the Si@SCS-1000-70 and Si@MCS-1000/1000-30 composites underlining the impact of the two-step thermal treatment as well as the silicon to carbon ratios.

For the first time we estimated the silicon fraction being initially accessible to the electrolyte by etching and elemental

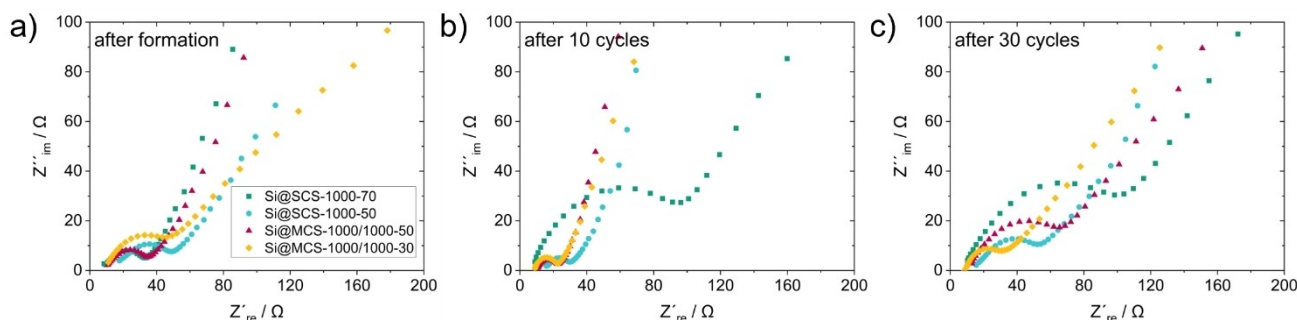


Figure 8. Nyquist plots of Si/C composites in CR2032 coin cells in a half-cell setup after formation, 10 cycles and 30 cycles.

analysis to quantify the efficiency of the embedding of silicon particles into a carbon shell or matrix. In Table S3 we summarize and compare publications evaluating silicon-carbon composites with multiple carbon shells showing a superior capacity retention at high specific capacities for our Si@MCS-1000/1000-30 composite.^[28,29,44,45] By using PAN as the carbon source for both carbon shells we were able to dedicate the positive effects to the improved composite structure. The comparably higher capacities and capacity retentions are very promising and an important step towards enabling silicon dominant anodes in lithium-ion batteries.

Conclusions

Our study demonstrates a simple and scalable method to manufacture Si/C composite particles for anodes in lithium-ion batteries. We found that the formulation and manufacturing processes of silicon-carbon composites (SCS or MCS) have a significant impact on the structural and electrochemical properties of Si/C composites. Through our research, we discovered that multiple carbon shell composites offer a more complete coverage of the silicon particle surface, which was verified through etching experiments and elemental analysis. Furthermore, our study contributes to establishing a method for estimating the surface coverage of silicon particles in Si/C composites, which allows for the determination of the initial fraction of silicon accessible to the electrolyte, which leads to unstable SEI formation and impedance growth. To the best of our knowledge such an approach has not been published before. The improved embedding process into the carbon structure through MCS composites provides an increase of the electric conductivity as well as reduced impedances and improved capacity retention during electrochemical evaluation. Our study offers valuable insights and paves the way for future research in the field of battery materials.

Experimental Section

Si/C Composite Preparation

Si/C composites consisting of a single carbon shell (Si@SCS) or multiple carbon shells (Si@MCS) were prepared. For SCS composites polyacrylonitrile (PAN, $M_w = 150000 \text{ g mol}^{-1}$, Sigma Aldrich) was dissolved in dimethyl sulfoxide (>99.9%, Sigma Aldrich) in a 1:4 mass ratio. Silicon nanoparticles (100–200 nm, CNPC Powder, 1.9 wt.% oxygen measured according to DIN EN 10276) were dispersed in the polymer solution using a laboratory mixer (Speedmixer DAC 150, Hauschild GmbH & Co. KG). The mass ratios of silicon and PAN were set to be 1:1 and 1:2 according to Table 1. The thermal processing was conducted in a chamber furnace (N7/H, Nabertherm GmbH) at 1000 °C for 12 h under nitrogen flow using heating rates of 1 K min^{-1} for temperatures below 300 °C and 10 K min^{-1} in the temperature range of 300 °C to 1000 °C. Multiple carbon shell composites were prepared by dispersing the Si@SCS-1000-70 composite in a second polyacrylonitrile solution (PAN: DMSO mass ratio 1:4) at Si: PAN ratios of 1:1 and 1:5 and performing a second thermal treatment under the above mentioned conditions.

Physicochemical Characterization Methods

Thermogravimetric Analysis (TGA) and Differential Scanning Calorimetry (DSC) were performed simultaneously with a NETZSCH STA 409 C/CD. The powdered samples were analyzed in an Al_2O_3 crucible between 25 °C and 1000 °C at a heating rate of 1 K min^{-1} while recording the sample temperature and heat flow (mW mg^{-1}).

Fourier-transform infrared spectroscopy (FTIR) was conducted using a Bruker Vertex 80v spectrometer with a HeNe laser emitting red light at 632.8 nm at a rated power output of 5 mW giving a spectral resolution of 0.2 cm^{-1} . IR spectra were recorded with 64 scans for background spectra and 32 scans for samples spectra. KBr pellets consisting of KBr and the sample in a 100:1 ratio were prepared and average values of triplicate measurements were used for the analysis.

A Bruker Senterra II confocal Raman spectrophotometer was used to analyze the composites with a 532 nm laser. The power was set to 0.25 mW using neutral density filters and spectra from 1000 cm^{-1} to 1800 cm^{-1} with a spectral resolution of 4 cm^{-1} were recorded with 500 coadditions of 10 seconds measurement time each. Gaussian-Lorentzian fitting was performed in Origin to calculate the degree of graphitization of the carbon shells (Figure S1). A Gaussian peak type was used for the G-, D_2 -, D_3 -, and D_4 -band and a Voigt peak type for the D_1 -band.

X-ray diffraction (XRD) measurements were conducted using a Rigaku Miniflex 600 with Cu K α radiation and a silicon monocrystal sample holder. The diffractogram was recorded between 10° and 80° 2 θ with a step size of 0.02° and a measurement time of 5 s per step.

Elemental Analysis (EA) was performed using a Vario MICRO Cube (Elementar Analysensysteme GmbH) in CHNS mode by sample combustion at 1150 °C in O₂ and quantitative measurement of the combustion gases N₂, H₂O, CO₂, SO₂. Sulfanilamide was used as the standard for the factor calculation.

Physisorption measurements were performed in a QuadraSorb Station 3 analyzer (Quantachrome Corporation) using nitrogen at 77 K. The sample was degassed for 16 h at 473 K prior to analysis. The specific surface area using Brunauer Emmett Teller (BET) theory and pore size distribution using density functional theory (DFT) were calculated using the QuadraWin software.

A custom-built set-up consisting of two copper stamps with a surface area of (A_{Cu}) 3.85 10⁻⁵ m² and a stamp holder made of polyether ether ketone polymer (PEEK) was used to determine the electric conductivity of the Si@SCS and Si@MCS composites. Samples of 75 mg composite were placed between the copper stamps which were subsequently pressed together at pressures between 0.3 and 5.5 MPa. For each pressure impedance spectroscopy was conducted between 1 Hz and 100 kHz at a sine amplitude of 5 mA. The specific conductivity σ was calculated using equation 2 (ρ is the bulk density of the powder composite, m the used powder mass and R the resistance measured).

$$\sigma = \frac{A_{Cu} \cdot \rho}{m \cdot R} \quad (2)$$

Scanning electron microscopy measurements (SEM) of the Si/C composites were recorded using an Auriga 60 CrossBeam Workstation (Zeiss Microscopy GmbH) with an in-lens detector (secondary electron (SE) detector) at a working distance of 4.5 to 5.5 mm and an acceleration voltage of 5 kV.

Scanning electron microscopy in transmission mode (SEM-TE) was performed on a Field Emission Gun High Resolution SEM (FEG-HRSEM) SU8220 instrument (Hitachi High-Tech Corporation) equipped with a transmission electron (TE) detector using an accelerating voltage of 30 kV.

Electrode Fabrication and Cell Assembly

Electrodes for analysis in half-cells were prepared containing 80 wt.% active material, 10 wt.% sodium alginate (Sigma Aldrich) binder and 10 wt.% carbon black (Super C65, MSE Supplies) and cast on a 9 μ m copper foil (MSE Supplies) using a doctor blade and a film applicator at a coating thickness of 60 μ m. A water-isopropanol mixture (20 wt.% isopropanol) was used as the solvent. After drying at 40 °C for >12 h, 14 mm coins were punched and subsequently dried under vacuum at 120 °C for >12 h. The mass loadings of all electrode coatings were found to be 0.8 \pm 0.1 mg cm⁻². Cells were assembled in an argon filled glovebox (E-Line, GS Glovebox System) in CR2032 coin cells using five layers of glass fiber separators (Whatman GF/A) and a lithium counter electrode at O₂ < 1 ppm, H₂O < 1 ppm. The electrolyte was prepared by adding 10 wt.% fluoroethylene carbonate (FEC, Sigma Aldrich) and 2 wt.% vinylene carbonate (VC, Sigma Aldrich) to a LP57 electrolyte (1 M LiPF₆ in EC: EMC 3:7 wt.%, E-Lyte Innovations GmbH).

Electrochemical Characterization

Electrochemical measurements were performed on a Neware BTS4000 series battery tester in the voltage range between 0.01 V and 1.5 V. Cell formation included one cycle at 200 mA/g (constant current, CC) followed by two cycles at constant current of 0.1 C based on the delithiation capacity of the first cycle. Subsequent CCCV (constant current constant voltage) cycling was performed at 0.5 C with a 0.1 C cut-off of the CV phase. For each material three cells were assembled and characterized. Electrochemical Impedance Spectroscopy (EIS) was conducted on a BioLogic BSC-805 cell tester in a delithiated state after formation and after every ten cycles during cycling at an AC amplitude of 10 mV in a frequency range 10 kHz to 10 mHz.

Supporting Information

The authors have cited additional references within the Supporting Information.^[28,29,44,45]

Acknowledgements

The authors thank Felix Leonard Gottwald for the SEM measurements, Christian Teske for the support with the XRD measurements and Svenja Kalthoff for the N₂ adsorption measurements.

This research was funded by the core funding of Fraunhofer Institute for Solar Energy Systems ISE (grantee D.B.) and the core funding of the University of Freiburg (grantee A.F.). In addition, parts of this work were funded by the Federal Ministry of Education and Research (BMBF) within the framework of the CarboBioElec project (013B1119A, grantee A.F.).

Open access funding was enabled and organized by Projekt DEAL. Open Access funding enabled and organized by Projekt DEAL.

Conflict of Interests

The authors declare no conflict of interest.

Data Availability Statement

The data that support the findings of this study are available from the corresponding author upon reasonable request.

Keywords: Anodes for Lithium-Ion Batteries · Lithium-Ion Batteries · NaOH etching · Polyacrylonitrile · Silicon-Carbon Composite

- [1] G. G. Eshetu, H. Zhang, X. Judez, H. Adenusi, M. Armand, S. Passerini, E. Figgemeier, *Nat. Commun.* **2021**, *12*, 5459.
- [2] Chunmei Ban, Kang Xu (Eds.) *Lithium-ion Batteries Enabled by Silicon Anodes*, The Institution of Engineering and Technology, London, **2021**.
- [3] C. Zhang, F. Wang, J. Han, S. Bai, J. Tan, J. Liu, F. Li, *Small Structures* **2021**, *2*, 2100009.
- [4] Z. Xiao, C. Wang, L. Song, Y. Zheng, T. Long, *J. Solid State Electrochem.* **2022**.

- [5] J. Li, J. R. Dahn, *J. Electrochem. Soc.* **2007**, *154*, A156.
- [6] B. Anothumakkool, F. Holtstiege, S. Wiemers-Meyer, S. Nowak, F. Schappacher, M. Winter, *ACS Sustainable Chem. Eng.* **2020**, *8*, 12788.
- [7] H. Schmidt, B. Jerliu, E. Hüger, J. Stahn, *Electrochem. Commun.* **2020**, *115*, 106738.
- [8] J. Wu, Y. Cao, H. Zhao, J. Mao, Z. Guo, *Carbon Energy* **2019**, *1*, 57.
- [9] M. Osiak, H. Geaney, E. Armstrong, C. O'Dwyer, *J. Mater. Chem. A* **2014**, *2*, 9433.
- [10] G. G. Eshetu, E. Figgemeier, *ChemSusChem* **2019**, *12*, 2515.
- [11] T.-W. Kwon, J. W. Choi, A. Coskun, *Chem. Soc. Rev.* **2018**, *47*, 2145.
- [12] J. Sun, L. Huang, G. Xu, S. Dong, C. Wang, G. Cui, *Mater. Today* **2022**.
- [13] C. Wölke, B. A. Sadeghi, G. G. Eshetu, E. Figgemeier, M. Winter, I. Cekic-Laskovic, *Adv. Mater. Interfaces* **2022**, 2101898.
- [14] S. Chae, S.-H. Choi, N. Kim, J. Sung, J. Cho, *Angew. Chem. Int. Ed.* **2020**, *59*, 110.
- [15] X. Dong, C. Lu, L. Wang, P. Zhou, D. Li, L. Wang, G. Wu, Y. Li, *RSC Adv.* **2016**, *6*, 12737.
- [16] J. Guo, A. Sun, X. Chen, C. Wang, A. Manivannan, *Electrochim. Acta* **2011**, *56*, 3981.
- [17] C. Li, C. Liu, W. Wang, J. Bell, Z. Mutlu, K. Ahmed, R. Ye, M. Ozkan, C. S. Ozkan, *Chem. Commun.* **2016**, *52*, 11398.
- [18] W. Liu, Y. Zhong, S. Yang, S. Zhang, X. Yu, H. Wang, Q. Li, J. Li, X. Cai, Y. Fang, *Sustain. Energy Fuels* **2018**, *2*, 679.
- [19] M. K. Datta, P. N. Kumta, *J. Power Sources* **2006**, *158*, 557.
- [20] M. Feng, J. Tian, H. Xie, Y. Kang, Z. Shan, *J. Solid State Electrochem.* **2015**, *19*, 1773.
- [21] N. Yusof, A. F. Ismail, *J. Anal. Appl. Pyrolysis* **2012**, *93*, 1.
- [22] D. Jang, M. E. Lee, J. Choi, S. Y. Cho, S. Lee, *Carbon* **2022**, *186*, 644.
- [23] M. Surianarayanan, R. Vijayaraghavan, K. V. Raghavan, *J. Polym. Sci. Part A* **1998**, *36*, 2503.
- [24] J. Kim, Y. C. Kim, W. Ahn, C. Y. Kim, *Polym. Eng. Sci.* **1993**, *33*, 1452.
- [25] E. Fitzer, W. Frohs, M. Heine, *Carbon* **1986**, *24*, 387.
- [26] D. Zhu, C. Xu, N. Nakura, M. Matsuo, *Carbon* **2002**, *40*, 363.
- [27] D. M. Piper, T. A. Yersak, S.-B. Son, S. C. Kim, C. S. Kang, K. H. Oh, C. Ban, A. C. Dillon, S.-H. Lee, *Adv. Energy Mater.* **2013**, *3*, 697.
- [28] N. Liu, J. Liu, D. Jia, Y. Huang, J. Luo, X. Mamat, Y. Yu, Y. Dong, G. Hu, *Energy Storage Mater.* **2019**, *18*, 165.
- [29] D. Vrankovic, K. Wissel, M. Graczyk-Zajac, R. Riedel, *Solid State Ionics* **2016**, *302*, 66.
- [30] Z. Wangxi, L. Jie, W. Gang, *Carbon* **2003**, *41*, 2805.
- [31] A. Sadezky, H. Muckenhuber, H. Grothe, R. Niessner, U. Pöschl, *Carbon* **2005**, *43*, 1731.
- [32] Y. Niu, X. Zhang, J. Wu, J. Zhao, X. Yan, Y. Li, *RSC Adv.* **2014**, *4*, 42569.
- [33] A. Samsul Kamal, N. Hafidzah Jabarullah, R. Othman, *Mater. Today: Proc.* **2020**, *31*, 211.
- [34] P. KLOBES, *Porosity and specific surface area measurements for solid materials*, FORGOTTEN BOOKS, [S.l.], **2022**.
- [35] M. Drews, J. Büttner, M. Bauer, J. Ahmed, R. Sahu, C. Scheu, S. Vierrath, A. Fischer, D. Biro, *ChemElectroChem* **2021**, *8*, 4750.
- [36] E. Buiel, J. Dahn, *ENHANCED ELECTROCHEMICAL CAPACITORS Selection of papers from the 1st International Symposium(ISEE'Cap09)* **1999**, *45*, 121.
- [37] L. Xie, C. Tang, Z. Bi, M. Song, Y. Fan, C. Yan, X. Li, F. Su, Q. Zhang, C. Chen, *Adv. Energy Mater.* **2021**, *11*, 2101650.
- [38] A. Gomez-Martin, J. Martinez-Fernandez, M. Rutttert, A. Heckmann, M. Winter, T. Placke, J. Ramirez-Rico, *ChemSusChem* **2018**, *11*, 2776.
- [39] A. Shellikeri, V. Watson, D. Adams, E. E. Kalu, J. A. Read, T. R. Jow, J. S. Zheng, J. P. Zheng, *J. Electrochem. Soc.* **2017**, *164*, A3914-A3924.
- [40] A. Wang, S. Kadam, H. Li, S. Shi, Y. Qi, *npj Comput Mater* **2018**, *4*.
- [41] S. J. Yeom, C. Lee, S. Kang, T.-U. Wi, C. Lee, S. Chae, J. Cho, D. O. Shin, J. Ryu, H.-W. Lee, *Nano Lett.* **2019**, *19*, 8793.
- [42] N. Zhang, Y. Zhang, T. Wang, W. Ge, T. Zhang, L. Zhang, W. Zhang, *J. Alloys Compd.* **2021**, *857*, 157530.
- [43] X. Bi, T. Tang, X. Shi, X. Ge, W. Wu, Z. Zhang, J. Wang, *Small* **2022**, *18*, e2200796.
- [44] H. Zheng, P. Lai, X. Tian, Z. Sun, Z. Zhang, *Energy Storage Science and Technology* **2023**, *23*.
- [45] F. Zhou, Z. Shang, X. Zhao, Q. Yu, Y. Mu, H. Xu, X. Tang, S. Huang, X. Li, *New J. Chem.* **2023**, *47*, 6313.

Manuscript received: January 10, 2024
Revised manuscript received: February 23, 2024
Accepted manuscript online: March 18, 2024
Version of record online: April 29, 2024